Mechanics & Industry 15, 413–426 (2014)

DOI: 10.1051/meca/2014049
www.mechanics-industry.org

Mechanics & Industry

Wear of WC-Co inserts in dry high speed machining of micron-sized particle aeronautical grade near β titanium alloy

H. Abdel-Aal[1,2,a] and M. El Mansori[3]

[1] Laboratoire de Mécanique et Procédés de Fabrication (LMPF), ENSAM CER Châlons-en-Champagne, Rue Saint Dominique, BP 508, 51006 Châlons-en-Champagne, France
[2] Ecpi University, 1001 Keys Drive, Greenville, SC 29651, USA
[3] École Nationale Supérieure d'Arts et Métiers, 2 cours des Arts et Métiers, 13617 Aix en Provence Cedex 1, France

Received 5 June 2011, Accepted 4 September 2012

Abstract – Current demands of higher damage-tolerance in the Aerospace industry resulted in resurging interest in β, or near β, titanium alloys. The combination of attractive properties of this class of alloys also led to the consideration of beta alloys for castings. Such alloys, however, are more difficult to cut than α-β titanium alloys due to their limited ability to work harden and the effect of β-stabilizers on ductility. These factors affect failure modes and active wear mechanisms of cutting inserts. This paper investigates some of the wear modes exhibited by WC-Co inserts when end milling the α near-β alloy Ti-x. In addition to being of near-β composition, this alloy is characterized by a fine sized microstructure (range of 1−5 μm). The study focuses on SEM and EDS observations of the wear patterns exhibited by two groups of inserts. The first is uncoated WC-Co, whereas the second is coated with multi layers of TiAlN. The results of this post-mortem study are compared to wear patterns, observed under identical conditions, while milling the α-β alloy Ti6Al4V. Results show that inserts used in machining the Ti-x alloy exhibit wear modes that contrast those exhibited when machining Ti64. The paper discusses factors leading to such occurrences and studies the influence of the alloy microstructure on tool effectiveness and failure modes.

Key words: Near Titanium alloys / WC/Co tools / titanium machining / wear of carbide inserts

1 Introduction

Elemental titanium is hexagonal close-packed at temperatures below 882 °C and is body centered cubic above this temperature. These phases are known as α and β respectively. Combinations of working and heat treatment alter the microstructure and change the mechanical properties of the metal. The microstructure and properties can also be affected by adding other elements to titanium. Addition of other elements to pure titanium i.e., alloying can alter microstructure and properties as well. Depending on which phase is to be dominant in a particular alloy (α or β) an alloying element (or group of elements) may be added to pure Titanium. Thus, one way of classifying alloying elements is according to whether they are α or β stabilizers. Alpha stabilizers are soluble in the α-phase and many act as solid solution strengtheners while also increasing the temperature at which the α-phase is stable. Alpha stabilizers include such elements as AI, Ga, Sn, Ge, and La. Beta stabilizing elements decrease the β transus (i.e., the temperature at which the material transforms to 100 percent β-phase). As such, these elements increase the range over which the β-phase is stable. Beta-stabilizers may be isomorphous or eutectoid. Isomorphous elements (such as V, Mo, Nb, Ta, and Re) are soluble in the β-phase while eutectoid elements like (Cr, Fe, Mn, Cu, Ag, Au, Ni, and Co) create an eutectoid phase.

A close look at beta stabili zing elements reveals that most of these are suited for high temperature applications. This is because they retain their strength at elevated temperatures. Thus, β-alloys offer potential advantages in terms of higher tensile and fatigue strengths, ability to heat treat greater section thicknesses to higher strength and enhanced formability [1]. On the other hand, β and heavily β-stabilized α-β, alloys offer considerable disadvantages. Among these are difficult weld ability, difficulty in damage tolerant applications due to unfavourable crack growth and toughness characteristics. In addition they possess high tendency to work harden thus they also cause great difficulties while formed into complex shapes.

[a] Corresponding author: hisham.abdelaal@gmail.com

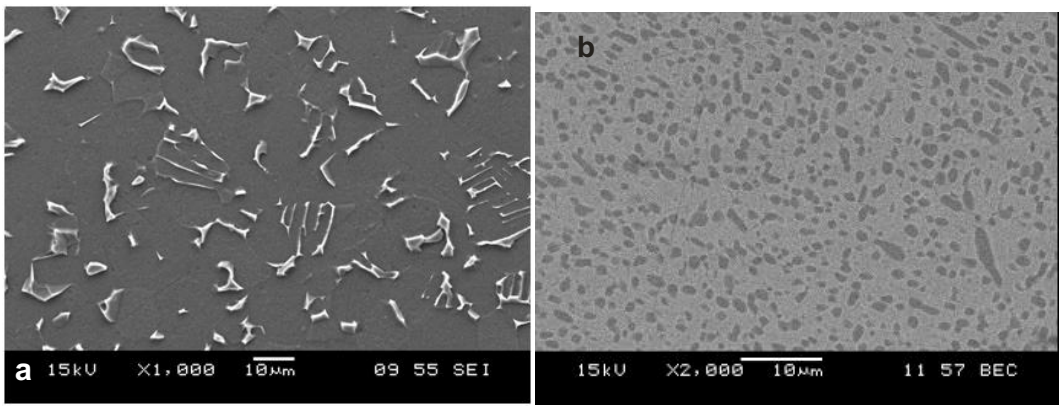

Fig. 1. Microstructure of workpiece alloys, (a) $\alpha + \beta$ alloy Ti-6Al-4V, (b) near β titanium alloy Ti-x.

Recent design considerations in the aerospace industry rejuvenated the interest in β-titanium alloys. Major air manufacturers, Airbus and Boeing, announced intended material changes for landing gear assemblies on their 787 and A350XWB airframes. Both manufacturers proposed the use of a near β-titanium alloy Ti_x-Al_x-Mo_x-V_x-Cr_x-Zr_x-Nb_x (this alloy will be referred to herein as β Ti-x for propriety reasons) which offers higher working strengths and wider processing window than the currently applied alloy (Ti-10V-2Fe-3Al) [2]. However, being of recent origin, there is a lack of information on machining of β- (or near β) alloys. This is despite the existence of information regarding thermomechanical processing of this family of alloys [3–6], and the availability of abundance of information regarding machining of titanium and some of its alloys (notably Ti-6Al-4V) [6–10].

Removal of material to achieve net shape is important in general. However, it assumes special importance in the case of the near β-Ti-x. This is because the applications envisioned for this entail large near net shape casting and forging which will require finishing through conventional machining operations. It is well known that titanium and titanium alloys are hard-to-cut materials. This means that Ti-x will most likely present engineers with many technical problems to be solved in order to produce net shape. Tool wear is likely to be one of the leading challenges to be overcome in machining this alloy. As such, study of the nature of tool wear when dealing with this alloy is needed. This paper is dedicated to such a purpose. Here we introduce the findings of a preliminary study of tool wear patterns when end milling the near β-alloy Ti-x. The work focuses on post mortem SEM observations of damage patterns in the used tools. To facilitate comprehension of the nature of damage results are compared to wear patterns observed when machining Ti-6Al-4V.

2 Experimental conditions

2.1 Workpiece material

Two alloys were chosen for end milling experiments: (a) Ti-6Al-4V (Ti64) duplex structure $\alpha/\alpha + \beta$, with average grain size (for both the α and $\alpha+\beta$) around 10 μm (range from 5 μm–20 μm), micro-hardness $HV_{0.2}$ 320 and, (b) Ti_x-Al_x-Mo_x-V_x-Cr_x-Zr_x-Nb_x(near β) with an average grain size around 1 μm (range from 0.5 μm−5 μm), micro-hardness $HV_{0.2}$ 380. Table 1 presents a summary of the chemical composition of both alloys.

Table 1. Chemical composition of workpiece alloys.

Element	Ti-6Al-4V % Weight	Ti-x % Weight
Al	5.5	4.5–5.5
V	3.8	4.5–5.5
Fe	Max 0.8	4.5–5.5
Mo	0	4.5–5.5
Cr	0	2.5–3.5
Nb	0	0.5–1.5
Zr	0	0.5–1.5

Figures 1a and 1b depict the microstructure of each of the workpiece alloys before machining. The initial microstructure of the Ti64 alloy (Fig. 1a), consists of single phase α grains with average grain size of 10 μm (range of 5 μm–20 μm). Inclusions of β grains are also seen. Similarly, the initial microstructure of the near β alloy Ti-x is shown in Figure 1b. The microstructure consists of single phase β grains with average size 5 μm (range 1 μm−5 μm).

2.2 Tool material

In this study we used coated carbide inserts made of Tungsten Carbide (WC) with 6% Cobalt (Co). All inserts had an applied single layer of TiAlN coating with average thickness 4 μm. Table 2 presents a summary of the mechanical and thermal properties of the cutting tools used, whereas Figure 2 depicts the microstructure of the cutting tool material.

All end milling experiments were performed in dry mode using a GSP 2108 R.20 variable speed Milling Machine with a 2 m maximum stroke. Table 3 presents a summary of the applied experimental parameters and the geometry of the tools used.

Table 2. Themomechanical properties of cemented carbides tools WC-6%Co.

Young modulus (GPa)	Poisson coefficient	Hardness (Knoop) (GPa)	density (kg/m^3)	Thermal conductivity (W/mK)	Thermal expansion at room temperature (10^{-6} K^{-1})
620	0.26	13	14 700	100	5

Table 3. Summary of the experimental parameters and tool geometry.

Cutting speeds V_c (m/min)	6	15	30	60
Feed f (mm/rev)	0.05–0.2	0.05–0.2	0.05–0.2	0.05–0.2
Tool geometry:				
Rake angle	0°, 5, 15, 30°	0°, 5, 15°, 30	0°, 5, 15°, 30	0°, 5, 15°, 30
Flank angle	6–7°	6–7°	6–7°	6–7°

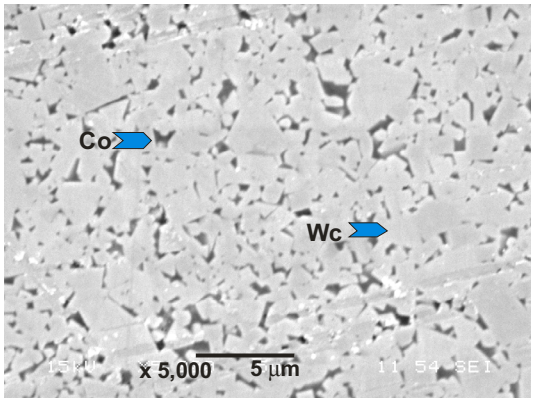

Fig. 2. SEM micrographs of tool material (WC-6%Co).

3 Results and discussion

In this section we report post mortem SEM observations of tool wear patterns. For comparison purposes we report observations for tools used in machining Ti-6Al-4V (referred to herein as Ti64) and for tools used in machining the near β alloy Ti_x-Al_x-Mo_x-V_x-Cr_x-Zr_x-Nb_x (referred to as Ti-x). All tool pairs reported were used under identical cutting conditions.

3.1 Reference state

Figure 3 (a through d) depicts the initial state of the unused inserts. The figure entails SEM imagery of two virgin tools. The tools shown in the figure have a 5° rake angle. Based on other images for tools with different rake angles (0, 15, 20, 30) it was judged that shown images fairly represent the virgin states of the tools used in this study. This is because no significant departure from the basic features presented in the figure was noticed in any tool with different rake angle. The figure depicts two types of tools: uncoated tools (shown in Figs. 3a and 3b); and a coated tool (shown in Figs. 3c and 3d). As stated earlier, the coating material is TiAlN and the thickness of the coating layer is around 4 μm. Two modes of imaging are presented for each tool: Secondary Electron Imaging (SE) (Figs. 3a and 3c), and Back scattering Images (BSE) (Figs. 3b and 3d). SE images reveal topological features of the surface. BSE images on the other hand reveal elemental chemical contrast. Thus, BSE images portray heavier elements (higher molecular weight) more illuminated than lighter (lower molecular weight) which will appear relatively darker.

Images of the uncoated tool (Figs. 3a and 3b) reveal two basic features. The first is the existence of parallel lines (skid grooves) of a variable depth that varies between (1−15 μm). These lines are parallel to the tool cutting edge. Such lines are residual of tool manufacturing procedures and die extrusion. The second feature meanwhile is the pre-existence of micro-craters close to the cutting edge. These minute-sized pits (order of 2 μm in diameter) are most probably cobalt granules (since they appear as darker spots in BSE images). Such entities, again, appear to be residual of the initial manufacturing procedures.

The coated tool (Figs. 3c and 3d) projects features that are similar to those observed in the uncoated tools. In particular, the presence of the parallel lines from extrusion procedures is almost identical to that appearing on the uncoated tool surface. The presence of micro-pits on the cutting edge is also a similar feature. Of interest, however, are the white quasi-spherical dots appearing on the surface of the tool. Higher magnification BSE images (see Fig. 3d) reveal that these features are rather blister-type protrusions that appear in the vicinity of the cutting edge. These are thought to be residual of the coating process. The diameter of these blisters ranges between 1 and 10 μm. Such occurrence is thought to impact the integrity of the coating through nucleation of localized coating delamination while machining.

3.2 Observations on worn tool

Figures 4 and 5 present images of the worn coated tools. Figure 4 (a through f), depicts Ti64 tools, whereas Figure 5 (a through f) depicts Ti-x tools. In each of the figures the state of three different tools is shown. The tools differ in the magnitude of the rake angle. Figures a, c and e of each image depicts tools with rake angles 5, 15, and 30 degrees, respectively. All tools were used for a cutting

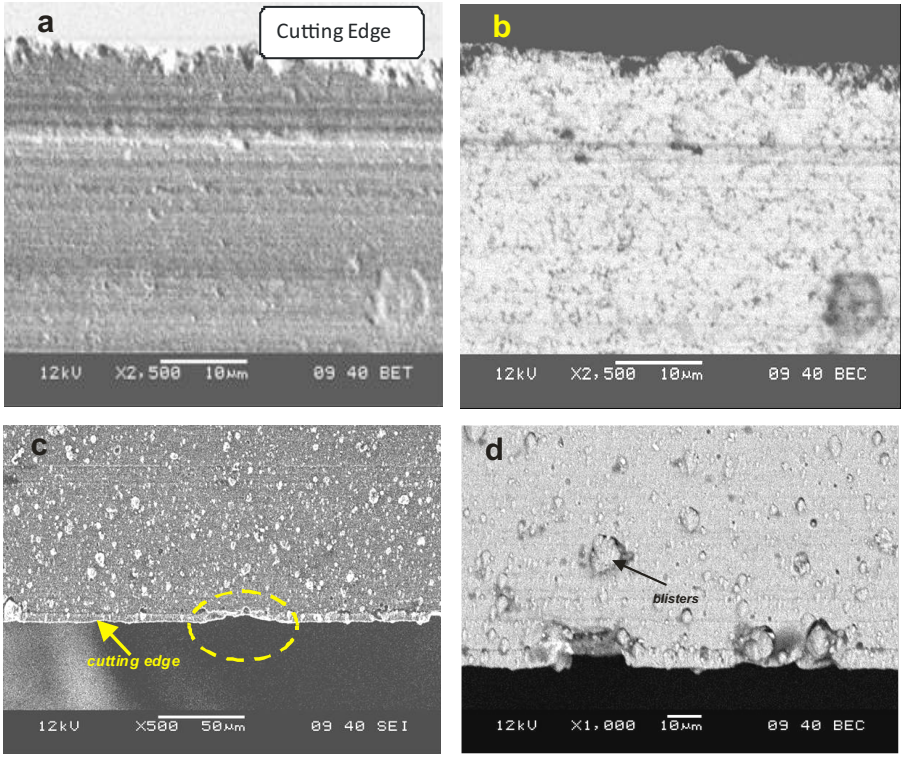

Fig. 3. SEM images of new uncoated and coated tools: (a) uncoated tool SE images, (b) uncoated tool BSE images, (c) coated tool SE image, (d) coated tool BSE images. Figure 3d is a magnification of the selected area in Figure 3c.

speed of 60 m/min and a feed of 0.2 mm. For each tool, in consistence with the presentation of the reference state, two contrasting images are presented: SE-mode imaging and BSE-mode imaging. Recall that with BSE images heavy elements (high molecular weight) appear more luminous than lighter elements (lower molecular weight). As such, within the group of tools examined (WC-CO) and TiAlN coating, the element Tungsten (W) should appear the brightest, titanium alloys (containing Fe and other heavier elements) will appear brighter than Ti by itself and less opaque than the coating material. Images designated b, d, and f of each figure are BSE images, whereas those designated a, c, and d are SE mode images.

3.2.1 General observations

Noticeable, on all of the tools examined, is the presence of surface irregularities on the cutting edge. These are more pronounced on the used tools than on the reference tools (compare Figs. 3a and 3c, 4a, 4c and 4e, and 5a, 5c, and 5e). The irregularities are due to attrition of the cutting edge of the two tool groups. In general, the intensity of attrition increases as the tool rake angle increases (regardless of the machined alloy), for example, if we compare the evolution of surface topography for each of the tool groups (Figs. 4a, 4c, and 4e for Ti64 and Figs. 5a, 5c, and 5e for Ti-x tools). In addition, it is noticed that surface damage for each of the tool groups entails more craters at higher rake angles. To clarify this observation, we introduce Figure 6. The figure presents SEM micrographs of the cutting edge for the tool sets shown in Figures 4 and 5. Figures 6 (a–c) pertain to the tools used in machining the Ti-64 alloy, whereas, Figures 6 (d–f) pertain to tools used in machining of the Ti-x alloy.

Comparing Figures 6b and 6c reveals that craters take place on the entire active edge of the 30° tool while only partial damage is noticed on the edge of the 15° tool. Figures 6 (e and f) display a similar trend to that observed for the Ti-64 tools. Chipping, however, is more pronounced for the 15° than the 30° Ti-64 tool.

The SEM micrographs in Figures 4 and 5 reveal the presence of un-identified particles of defined edges. Initial inclination is to consider these particles as residue carbide particles that migrated to the surface during machining. However, BEC images indicate that such particles belong to a very light material (they appear floating over the surface in BET imagery). Such behavior is inconsistent with the behavior of carbide particles. As such, to verify the origin of these particles we performed Elemental Particles Analysis (EPS) on two tools. The results are presented in Figures 7 (a–d) and 8 (a–d). Figure 7 presents the results for a tool used in machining the Ti64 alloy whereas, Figure 8 presents the results for a tool used in machining the Ti-x alloy.

The analyzed regions were chosen so that they contain damaged as well as unaffected zones of the tool. In such a way, changes in the composition of the carbides may be detected. Four plots are supplied in each figure. These are: region of analysis (Figs. 7a and 8a); mapping of the

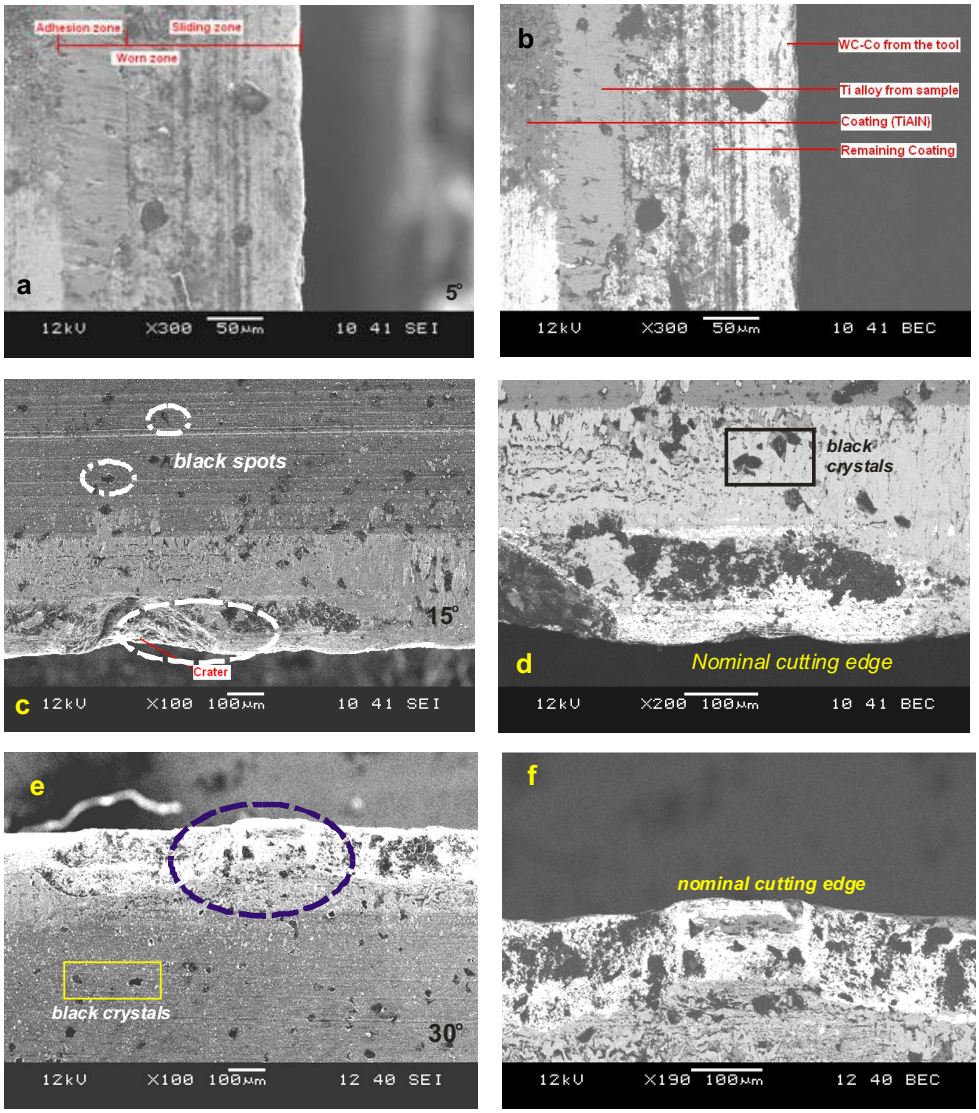

Fig. 4. SEM images for a group of tools used in machining Ti-6Al-4V. Cutting conditions $V = 60$ m/min, feed = 0.2 mm/rev. Figures 4a, 4c, and 4e – Ti64 SEI images tool angles: 5° 15°, 30°, respectively. Figures 4b, 4d, and 4f BEC images. Note that the scale for BSE images is higher than that for the SEI images. Figures 4 (d and f) are magifications of the selected zones in figures (c and e respectively).

elements within the analyzed region (Figs. 7b and 8b); the spectrum of the elements detected within the chosen region (Figs. 7c and 8c); and the percentage of the elemental composition in the analyzed region.

For both tools, EPS did not reveal significant changes in composition nor an odd local concentration of particular constituent element (see Figs. 7a, 7b and 8a, 8b). Further, the relatively invariant percentages of the elements Tungsten (W), Cobalt (Co), and Carbon (C) (see Figs. 7d, and 8d), suggest that the observed particles are foreign to the carbides (i.e., they are of extrinsic origin). This is confirmed by the presence of traces of the elements Chlorine (Cl), Potassium (K), and Sodium (Na). The presence of such elements suggests that the particles in question originate from the india-ink used to mark individual inserts before experimentation. The ink may have evaporated due to the heat generated in machining and residues smeared the tool.

3.3 Observations on material transfer

Build-up through material transfer from the workpiece material to tool surface is visible for both tool groups (especially upon studying BSE images). The transfer layer, moreover, grows with the increase of the rake angle. BSE images also reveal that coating delamination is an active mode of tool failure. It is beneficial to compare the location of delamination in the used tools with the general location of the blisters observed in the virgin coated tools. Delamination is more visible for the Ti64 tool group. Observe, for example (Fig. 4b),

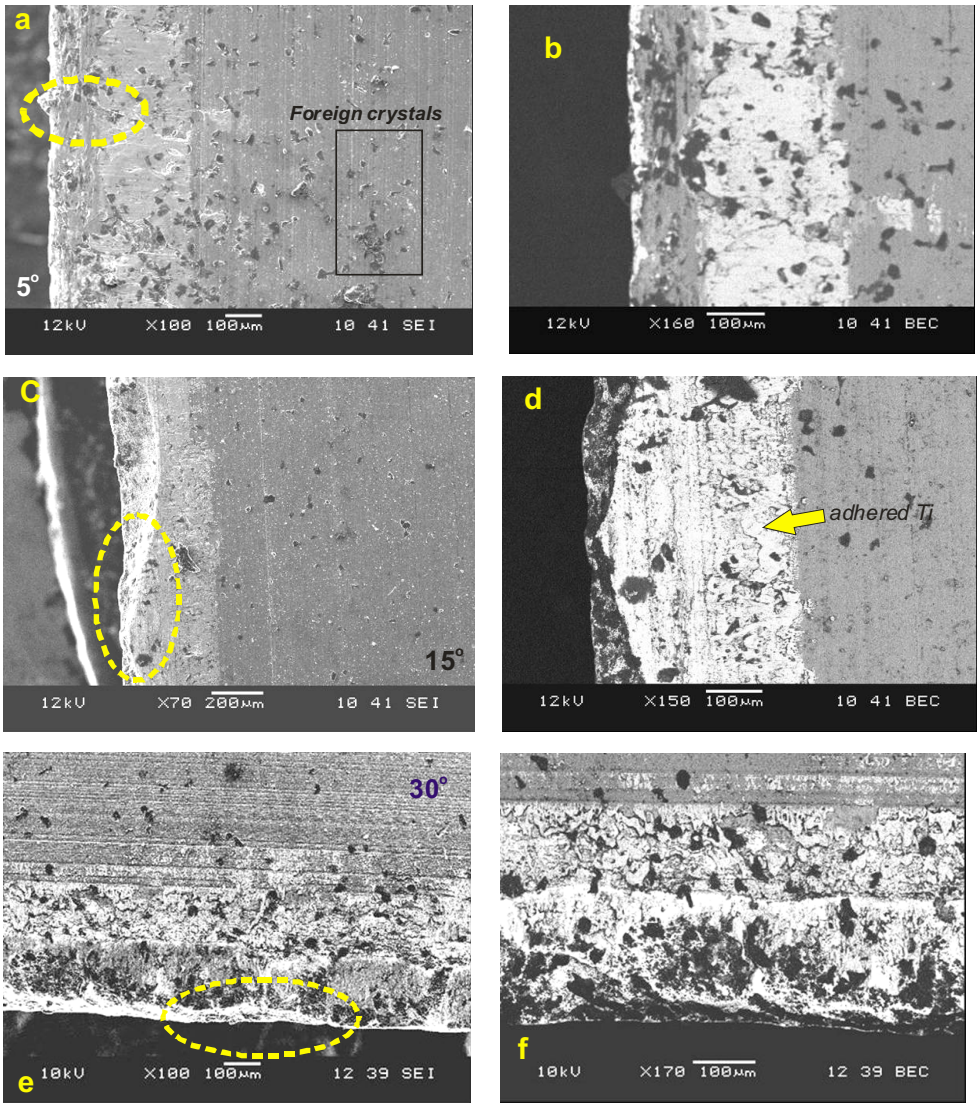

Fig. 5. SEM images for a group of tools used in machining Ti-X. Cutting conditions $V = 60$ m/min, feed $= 0.2$ mm/rev. Figures 5 (a, c, and e) – Ti64 SEI images tool angles: 5°, 15°, 30°, respectively. Figures 5 (b, d, and f) BEC images. Note that the scale for BSE images is higher than that for the SEI images. Figures 4 (b, d, and f) are magifications of the selected zones in figures (a, c, and e respectively).

where the active length of the tool contains remnants of the original coating. The delamination zone is followed by an adhesion-dominated zone through which the workpiece material forms an elevated layer on the rake face. Further study of the images presented in Figures 4 and 5 indicates that the active part of the tool comprises two regions. A characteristic length represents the width of each of the regions. Thus, we define two distinct lengths. The first length, designated L1, starts from the boundary of the cutting edge of the tool and extends to the upper boundary of the adhesion zone. The second, designated as L2, represents the width of the adhesion zone (i.e., defined here as the area that is dominated by material transfer from the workpiece to the rake face due to chip sliding). Figure 9a depicts each of the defined lengths. In what follows we will refer to the length L1 as the delamination length and the length L2 as the adhesion length.

Image analysis of SEM graphs and WLIs yielded an estimate for the adhesion and the delamination lengths for each of the tools examined in this work. In estimating the delamination length, we considered the thickness of the area showing signs of coating delamination whether it being continuous or intermittent. To estimate the length L1 first there is a need to establish the original cutting edge of the tool (before being worn). As shown in Figures 9b, and 9c, the location of this reference line (datum) is assumed to be located where the zero level is given from WLI. Following the location of that reference line, the lengths L1 and L2 are located based on the vertical topography of the active zone of the tool (Fig. 9c). Consequently, the measurements presented herein are qualitative in nature. Nevertheless, these estimates yield a fair perspective of damage progression both as a function of tool geometry and as a function of workpiece material.

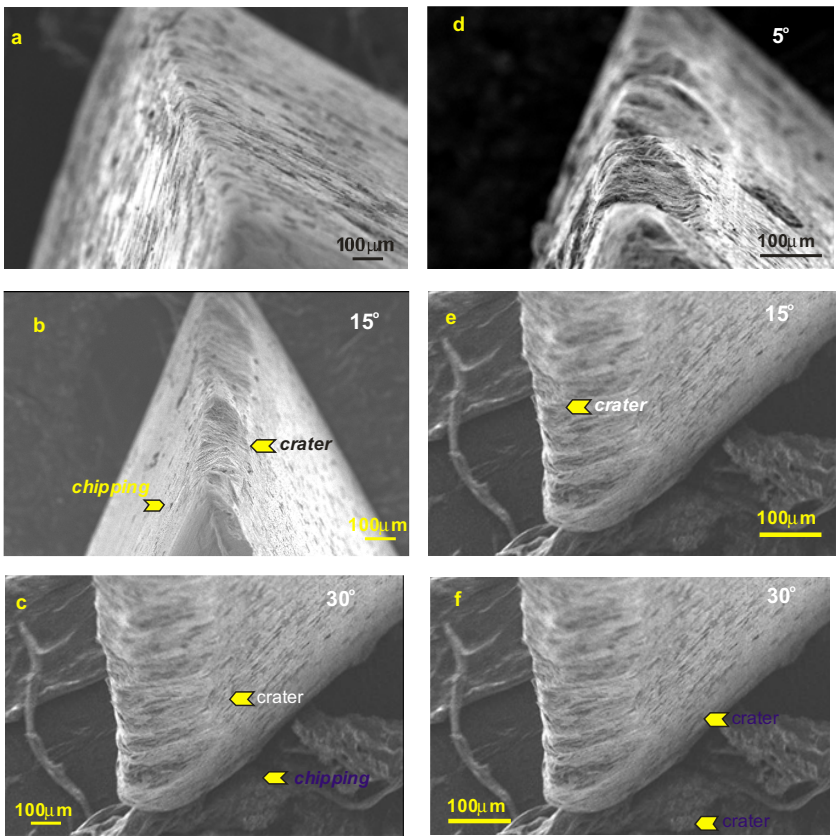

Fig. 6. SEM micrographs of the cutting edge for the tool sets shown in Figures 4 and 5. Figures 6 (a–c) depict tools used in machining the Ti-64 alloy, whereas, Figures 6 (d–f) depict tools used in machining of the Ti-x alloy. Cutting conditions $V = 60$ m/min, feed $= 0.2$ mm/rev.

Figure 10 depicts the evolution of the scales L1 and L2 with the rake face angle of the tool. Figure 10a depicts the variation in the delamination length, L1, for both tools. Meanwhile, Figure 10b depicts the evolution of the adhesion length, L2. For all rake angles used, the width of the delamination region (Fig. 10a), for the Ti-x tools is slightly higher than that estimated for the Ti64 alloy. The adhesion zone for the Ti-x tools is also wider than that estimated for the Ti64 tool group (except for the 5-degree rake angle tool).

3.4 Surface profile observations

White Light Interferometery (WLI) measurements confirmed the general trend of scales L1 and L2. Figure 11 (a through d) depicts WLI scans of two tool groups of identical geometry, 0° rake angle. The first group (shown as Figs. 11a and 11b) was used at a cutting speed of 15 m/min whereas the second was used at a speed of 60 m/min (shown as Figs. 12a, 12b). Figure 11a depicts measurements of the adhesion zone for the Ti-x tool and Figure 11b depicts the Ti64 tool. Again we note that the width of the adhesion band in case of the Ti64 tool is narrower than that of the tool used with Ti-x. The height (thickness) of the build-up layer above the tool surface is greater in case of the Ti64 tool than that for the Ti-x tool (5 μm as opposed to 1 μm). The trend of width for the delamination band is also consistent with those found from SEM image analysis (see Figs. 12a, and 12b).

An indication of surface damage intensity in both tool groups is revealed through WLI. Figure 13 depicts an SEM of two tools. The first was used with the Ti64 alloy, shown as Figure 13a, and the second was used with the Ti-x alloy, shown as Figure 13b. Both tools have 15 degree rake angle and were used at a speed of 60 m/min and a feed of 0.2 mm. Figure 14 depicts the WLI scans for both tools. Figure 14 (a, c, and e) represents the Ti64 tool and Figure 14 (b, d, and f) represent the Ti-x tool. The figure indicates that the intensity of surface damage in case of the Ti-x alloy is more pronounced than that observed on the Ti64 alloy. Chipping also is noticed at the edge of the Ti-64 tool. Interestingly, the thickness of the adhesion zone (height above the surface) is higher in case of the Ti64 than in case of Ti-x.

Wear mechanisms noted on Ti64 tools are familiar failure modes pertaining to WC/Co tools when milling titanium alloys. In particular chipping (see Fig. 13), is frequently a major failure mode for such tools [9]. This mode of wear results from a combination of high temperature and high thermo-mechanical stresses as well as adhesion of workpiece material onto the tool faces [11]. All of these inhibitors were observed on the Ti64 tool group.

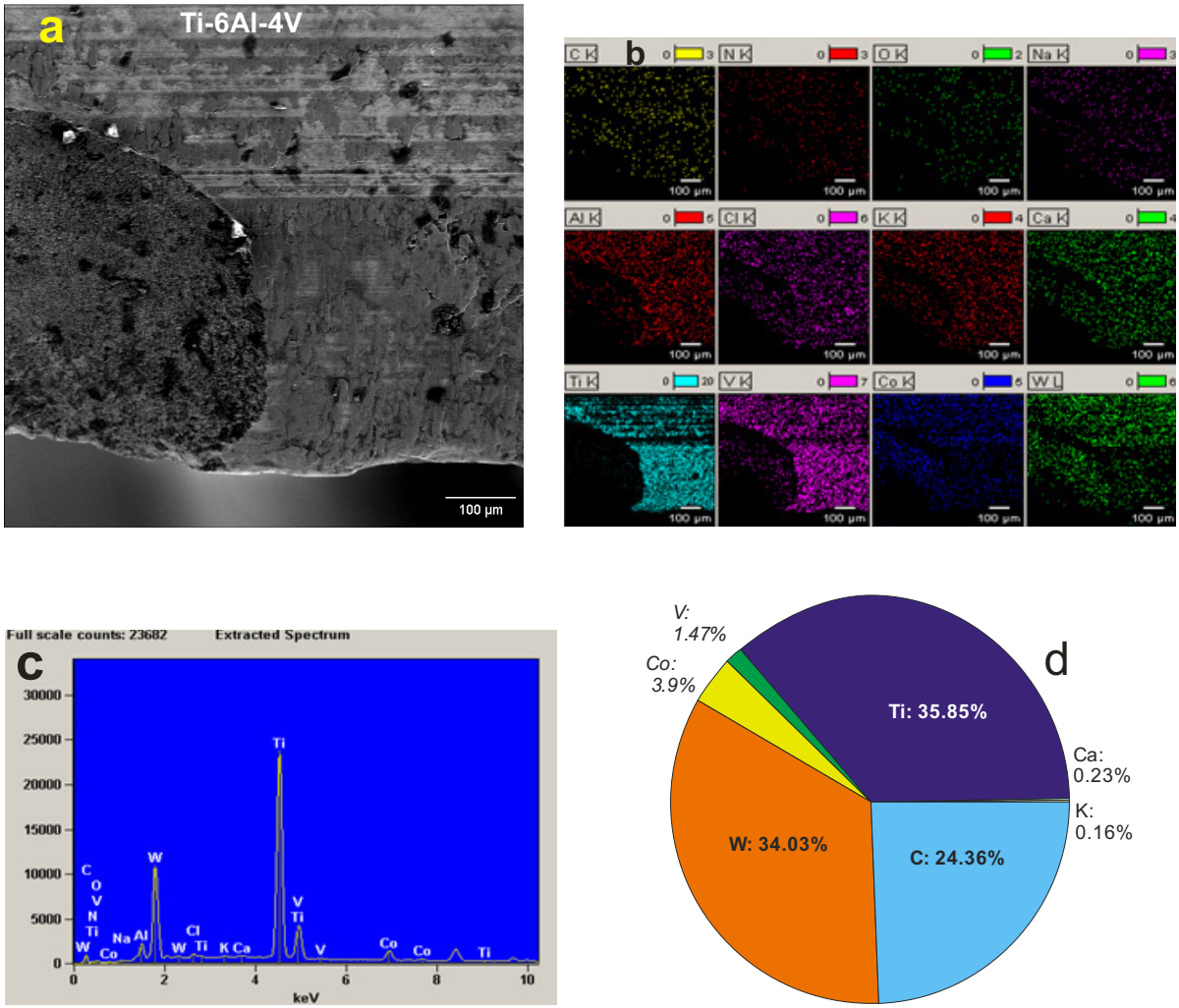

Fig. 7. Analysis of the damaged zone of a tool used for machining the Ti-64 alloy (rake angle = 5°, V = 60 m/min, and f = 0.2 mm/rev). (a) SEM micrograph of the zone of analysis, (b) mapping of the detected chemical elements found in the selected zone, (c) chemical spectrum of the detected elements, and (d) pie-chart representing the percentage of all elements detected within the zone of analysis.

Chipping, however, was not observed for the Ti-x tool group, although crater wear and adhesion were observed (Fig. 13b). One explanation of this observation may be rooted in thermal behaviour.

Temperature is the catalyst of the majority of tool wear mechanisms [12]. The temperature of the cutting edge, other factors being equal, will depend on the thermal conductivity of the tool material. A comparison of the thermal conductivities of Ti64 and Ti-x (7−14 W/mK (293 K $< T$ 1000 K), for the former and 14−21 W/mK (293 K $< T <$ 800 K) for the later [13]) indicates that at identical cutting conditions the temperature rise for the Ti64 alloy is likely to be higher than that for the Ti-x alloy. This will produce an environment that is less conducive to chipping when machining Ti-x. Another indicator of the importance of the thermal behaviour is the trend of the adhesion length L2. This scale was found to be higher for Ti-x more than that for Ti64. This, points at higher intensity of temperature (rate of temperature rise) on the contact length of the Ti64 tool. Temperature concentration within an area promotes both adhesion and diffusion. More interestingly, the role of thermal conductivity here is very important.

Material transfer from the workpiece to the rake face of the tool is a function of the temperature rise due to sliding of the chip on the rake face. A consequence of the temperature rise is a change in the thermal properties of both workpiece and tool materials. Of these, the change in the thermal conductivity is more influential on the account of the coupling between these two properties through their electronic origins [14,15].

The electron fluid in a metal is an excellent conductor of electrical charge. It is also an excellent conductor of heat. In an insulator, phonons (quantized lattice vibration) carry all the heat current. By contrast, in familiar metals, the electron fluid conducts nearly the entire heat current (the phonon current still exists but constitutes an extremely small percentage of the total heat current).

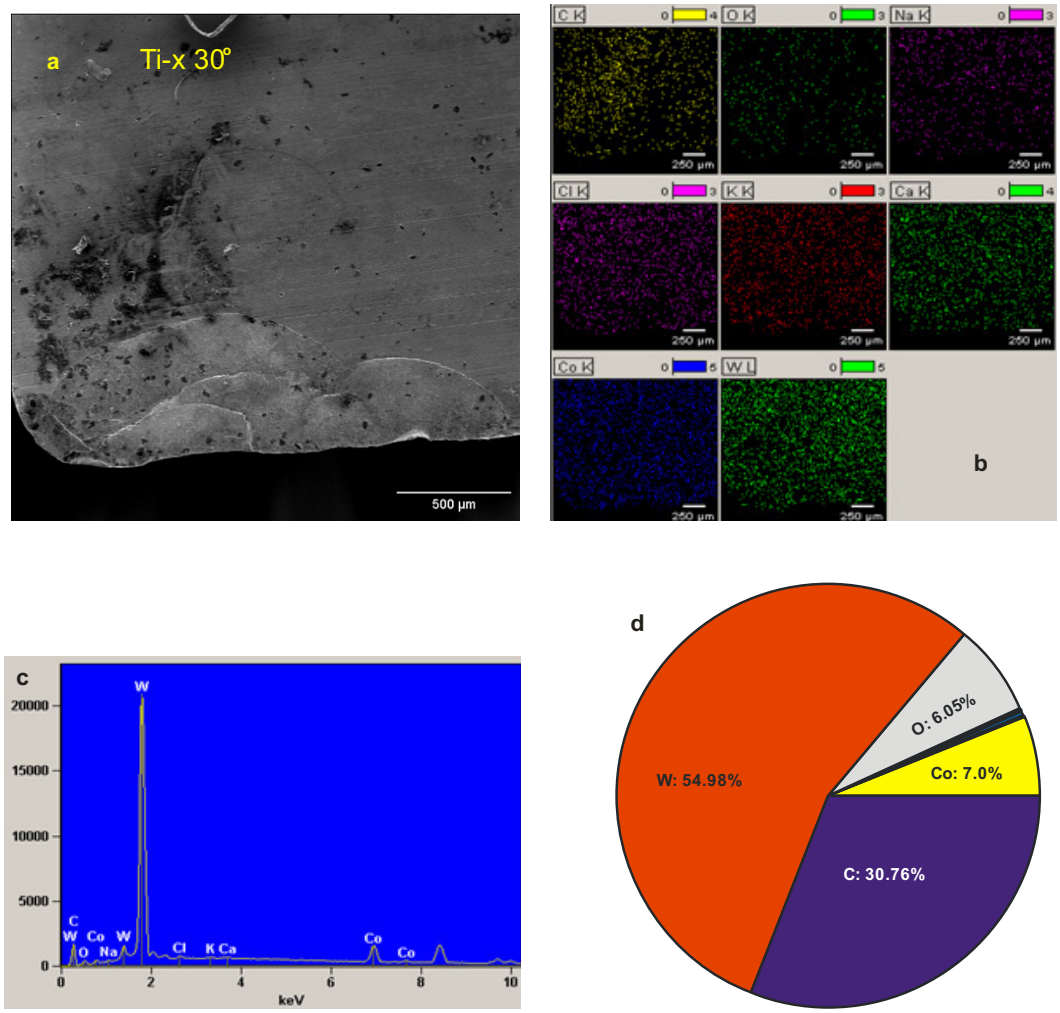

Fig. 8. Analysis of the damaged zone of a tool used for machining the Ti-x alloy (rake angle = 5°, V = 60 m/min, and f = 0.2 mm/rev). (a) SEM micrograph of the zone of analysis, (b) mapping of the detected chemical elements found in the selected zone, (c) chemical spectrum of the detected elements, and (d) pie-chart representing the percentage of all elements detected within the zone of analysis.

Since the electrical and thermal currents carry distinct quantities (charge and entropy) it is interesting to compare their magnitudes. Gustav Wiedemann and Rudolph Franz undertook the earliest comparison between these magnitudes in 1853. They found that, in metals, the ratio of the thermal to electrical conductivity is constant. Following such a discovery, Ludvig Lorenz in 1872, found that the same ratio may be expressed as a temperature dependent quantity, whence the Wiedemann-Franz-Lorenz (WFL) law, i.e.

$$\frac{K}{\sigma T} = 2.45 \times 10^{-8}\ \mathrm{W}\ \Omega\ \mathrm{K}^{-2} \tag{1}$$

where K is the thermal conductivity, σ is the electrical conductivity, and T is the temperature. The constant in equation (1) is universal and is not affected by stress or pressure [16].

The sliding of the created chip on the rake face of the tool causes the generation of an electrostatic potential due to the phenomenon of "tribo-electrification". The strength of the resulting potential is may be calculated from [17],

$$\Phi(T) = \left[\frac{1}{2}\int_{T}^{T_{\max}} \rho(T)\, k(T)\, dT\right]^{1/2} \tag{2}$$

where ρ is the electrical resistivity (reciprocal of the electrical conductivity $\rho = 1/\sigma$).

Equation (2) implies that the strength of the potential resulting from the sliding of the chip on the rake face depends on the values of the electrical resistivity and thermal conductivity along with their variation with temperature. The integration in equation (2) proceeds from the inside toward the surface, i.e., along the path WS on the workpiece and along the path TS on the tool as illustrated in Figure 15.

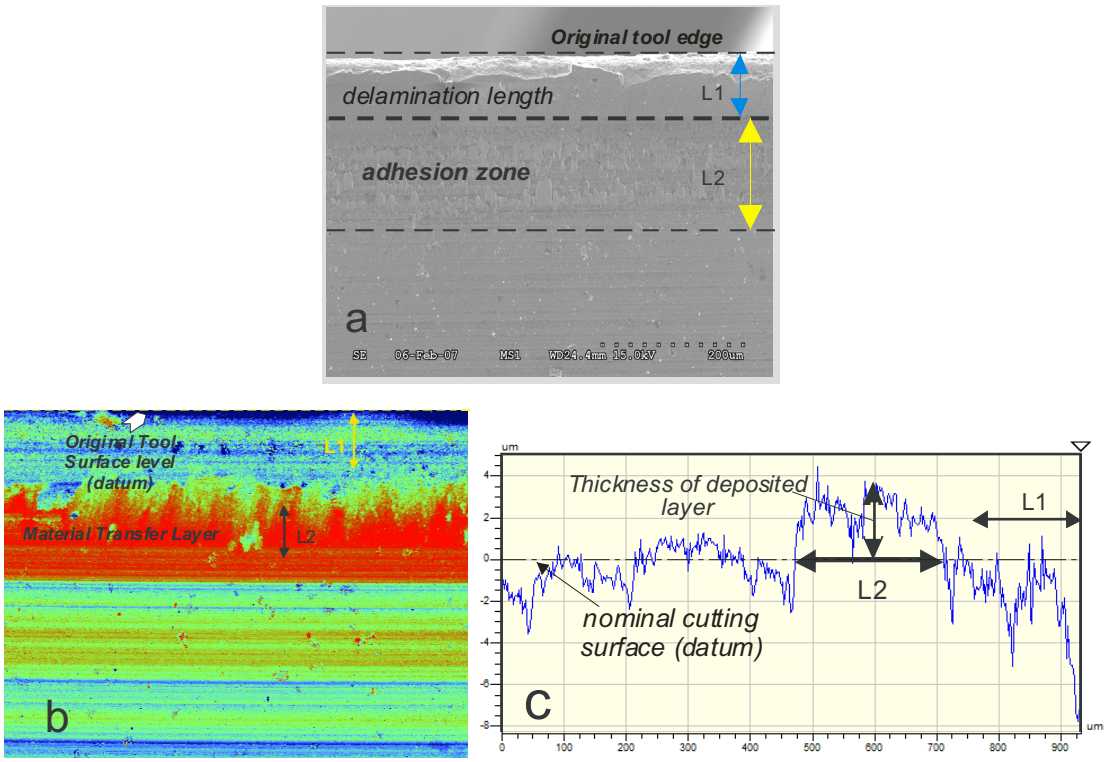

Fig. 9. Illustration of the delamination length (L1) and the diffusion length (L2). (a) definition of the characteristic lengths L1 and L2 on an actual worn tool, (b) WLI scan of the active zone of the tool and collocation of the various zones on the scan, (c) Y-axis profile of the active zone of the tool, note that the reference datum for estimating L1 and L2 is located at Zero thickness.

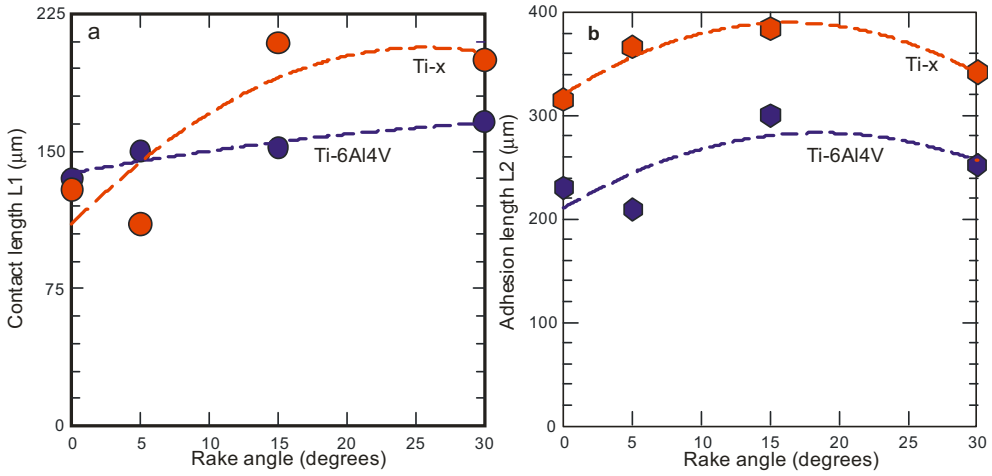

Fig. 10. Evolution of the delamination width scale L1 and the adhesion width length scale L2 with rake angle at 60 m/min.

Substituting from equation (1), we may write:

$$\Phi(T) = \left[\frac{1}{2}\int_{T}^{T_{\max}} CTdT\right]^{\frac{1}{2}} \tag{3}$$

where C is the WFL constant given by equation (1). Equation (3) integrates to:

$$\Phi(T) = \sqrt{\frac{C}{2}}\left[T_{\max}^2 - T^2\right]^{\frac{1}{2}} \tag{4}$$

Equation shows that the strength of the developing potential depends on the difference between the square of the surface temperature and the temperature in the inside of the material. This difference, on the other hand, depends, in part, on the thermal conductivity of the particular materials and the manner it drops with temperature elevation. As such, if the Ti64 and the Ti-x alloy are machined by the same WC-Co tool, all other conditions are equal, the Ti-x alloy will develop a stronger electrical potential.

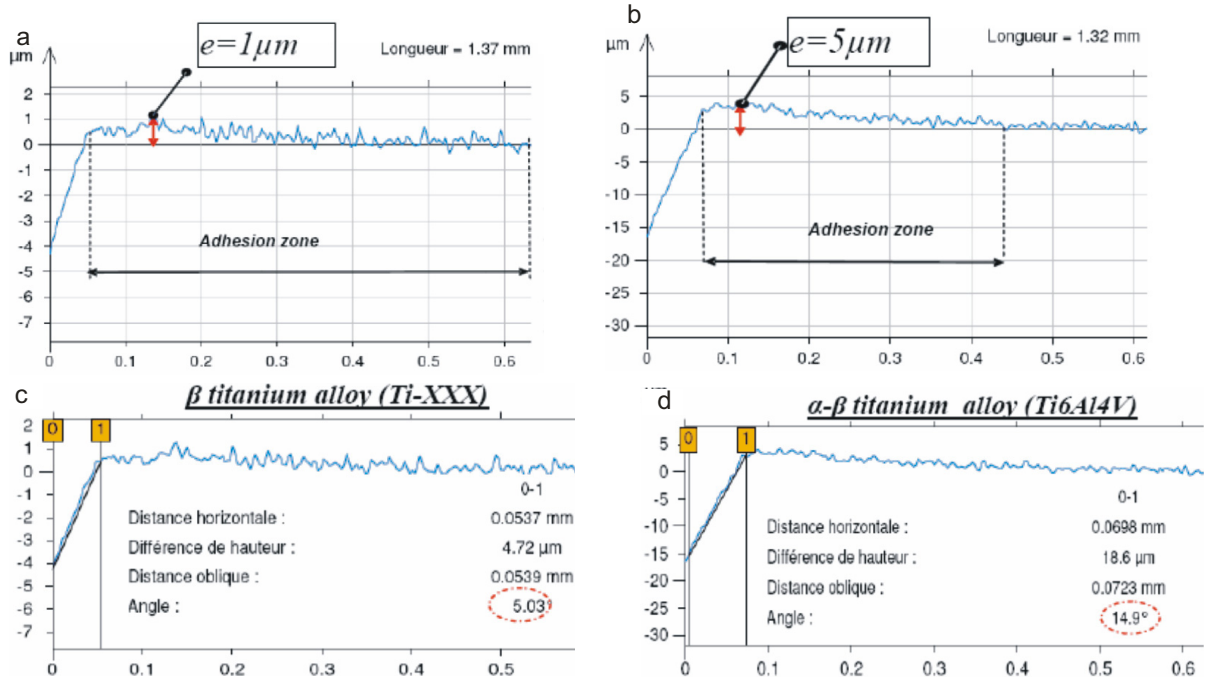

Fig. 11. Surface analysis: Adhesion wear and built-up-layer for coated WC-Co./Ti-Al-N, cutting speed $Vc = 15$ m/min, rake angle 0°.

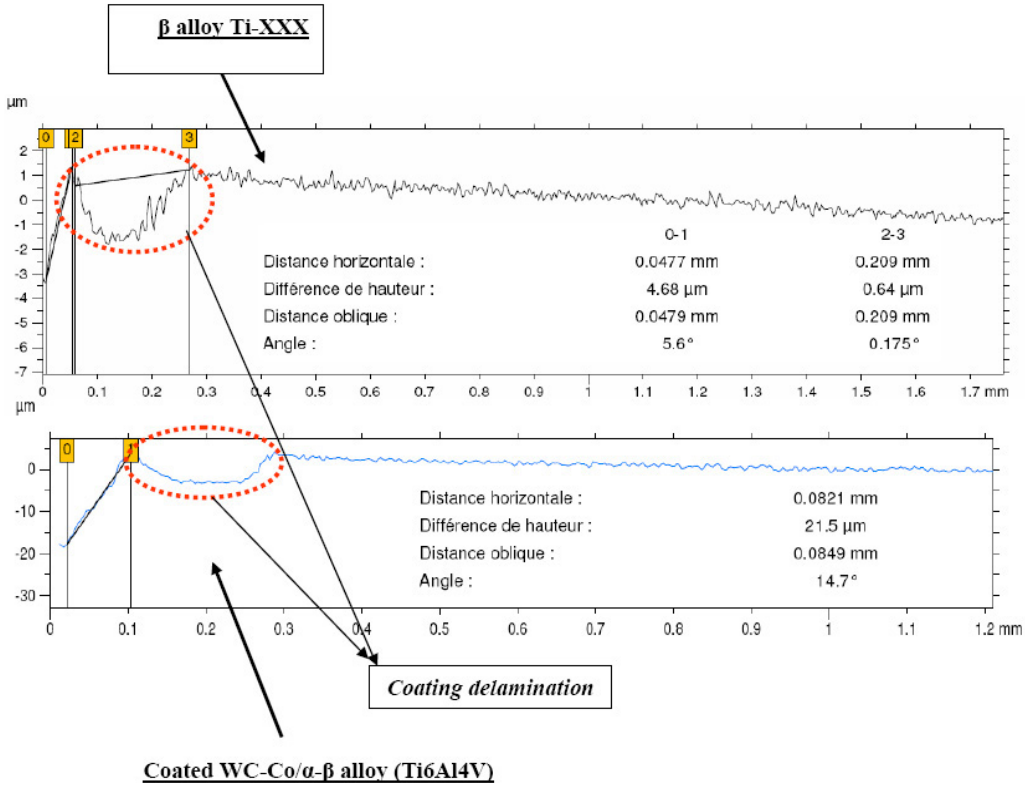

Fig. 12. Surface analysis: coating delamination for coated WC-Co./Ti-Al-N, cutting speed $Vc = 60$ m/min, rake angle 0°.

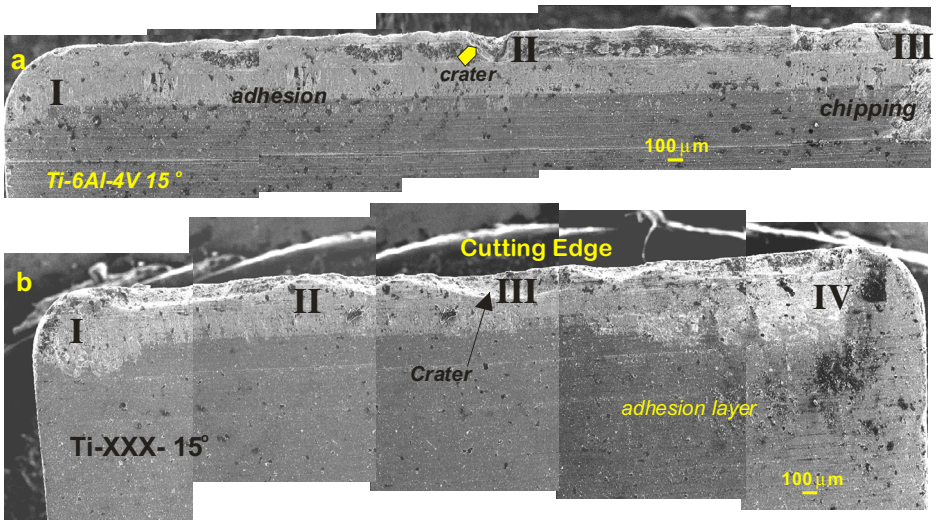

Fig. 13. Full SEM images of damage suffered by the active part of two tools: (a) tool used with Ti6Al4V, (b) tool used with Ti-x. Machining conditions $V = 60$ m/min, feed $= 0.2$ mm/rev.

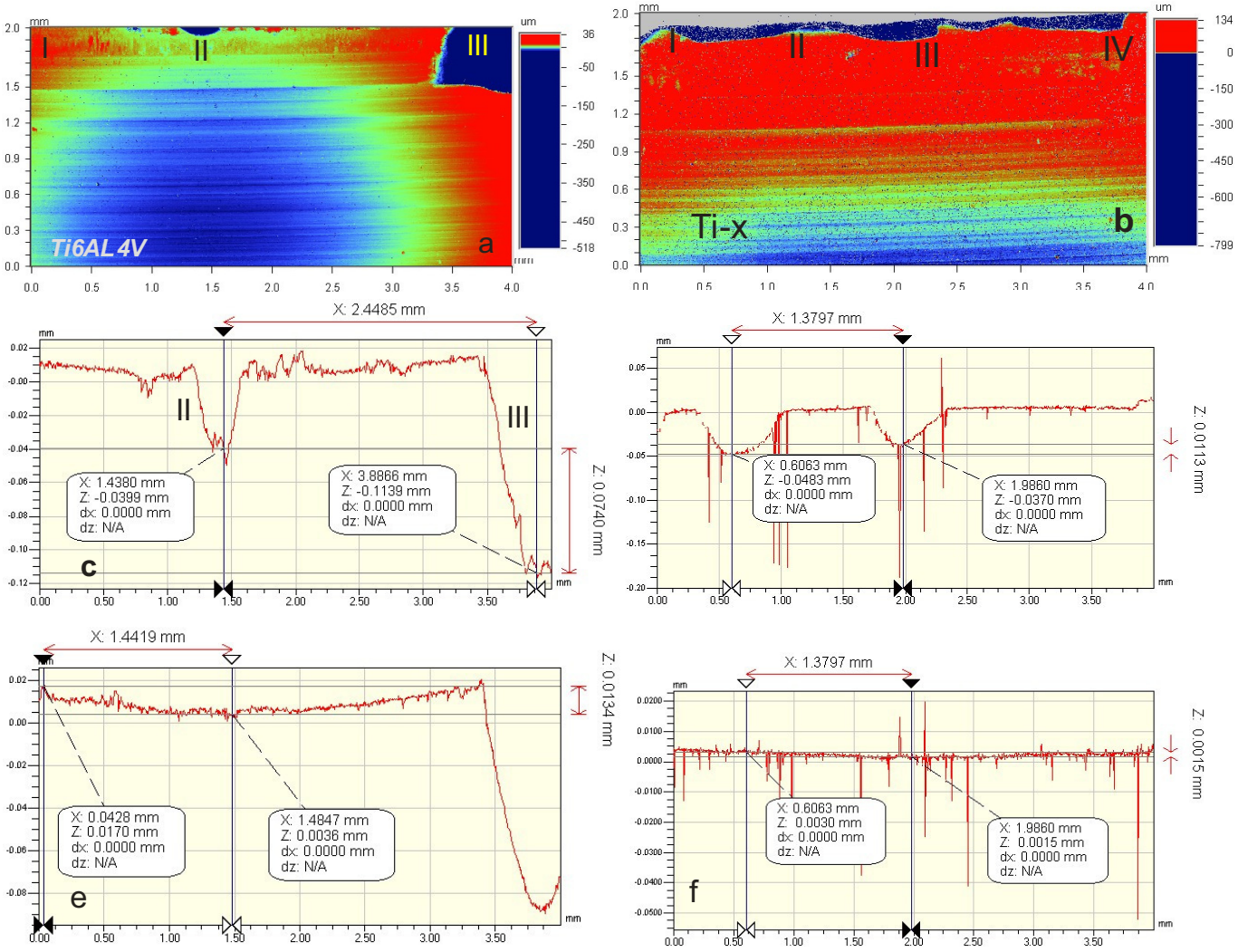

Fig. 14. White Light Interferometery WLI scans for tools shown in Figure 13. (a) General surface topography Ti64, (b) general surface topography Ti-x, (c) cutting edge profile Ti64, (d) cutting edge profile Ti-, (e) Adhesion profile Ti64, (f) adhesion profile Ti-x.

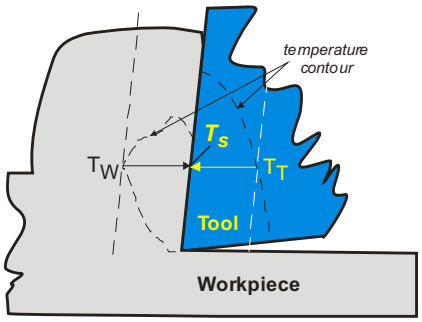

Fig. 15. Schematic illustration of the integral paths for equation (2).

Now the direction of the material transfer follows the direction of the gradient between potential developed on tool and that developed on workpiece [18]. It follows that the direction of the discharge force assisting material transfer in the case of the Ti-x alloy will be smaller than that developed in case of the Ti64 alloy whence the difference noted in the adhesion.

A connection between adhesion length and transport properties was hypothesized in the work of Friedman and Lenz [19,20] who reasoned that since the temperature affects the contact length between chip and tool; and since the temperature itself is affected by thermal conductivity, then thermal conductivity should affect the contact length. They further noticed that the location of the maximum temperature, in the contact length between chip and rake face, occurs in the trailing half of the contact. Such an area in their experiments represented the general area where transition from secondary deformation to sliding took place. As such, Friedman and Lenz suggested that the extent of adhesion length depends on the temperature developed on the interface of chip and rake face. This, again, is inversely proportional to the thermal conductivities of the materials involved. Therefore, for the higher conductivity material, Ti-x, the temperature developed will be lower than that developed for the lower conductivity material, Ti64. This will result in an adhesion length, L_2, that is higher for the Ti-x alloy than that for the Ti64 alloy.

Extrapolating from the work of Jones et al [21] on similar near β-alloy the Ti-x alloy is likely to display negligible flow at high temperatures. This implies that at higher speeds, and associated higher temperatures, the Ti-x alloy will not soften as desired. This will require higher stresses to generate net shape surface or remove specific material volume. As such, tool wear will intensify for the Ti-x alloy more than that for the Ti64 alloy. The envisioned mechanism for the increase of wear is rooted in the effect of the high contact stress between tool and active material zone in the work piece.

During machining, elevated pressures and temperatures dominate the active volume of the work-piece. The active zone of the tool and the workpiece will display local baric and temporal variations, which may lead to complex responses. These synergetic effects will dominate within the enclave of material located directly under the tool. Based on the derogatory influence of pressure on thermal conductivity titanium [22] one may conclude that behavior of the workpiece, and the energetics of workpiece-tool interaction will be governed by the upper limit of the pressure reached upon tool engagement.

The initial (actual) contact pressure between tool and work piece will be the primary factor that determines the trajectory of thermal and electrical transport in the active zone throughout the duration of machining. Any fresh material engaging the tool will be affected by the pressure history more than the thermal history of the contact. This will lead to a higher degree of coupling between thermal and electrical effects within the contact. To the effect, that further reduction in the ability of the active zone for heat dissipation will take place. A reduced ability to conduct heat (i.e., lower effective thermal conductivity due to higher stress) leads to higher resistance to electrical flow (at the same temperature). Taking into account that the mode of damage to both tool and workpiece relates to the favourable mode of energy dissipation under the particular contact conditions, then the coupling between electrical and thermal transport becomes influential. When the ability of the active material zone to conduct heat is reduced, energy dissipation through electrical influences will be more active. Thus, electrical currents, and the evolution of associated electro-static potentials, will be energetically favourable. If the strength of the potentials evolving on the tool side is different from that evolving on the work piece side, then a discharge force will take place in the direction of the potential gradient. Such a force will trigger higher stiction, adhesion and thereby material transfer between tool and work piece (whence intensifying damage).

Conclusions

In this work we presented a study for the wear of WC-Co inserts when machining two types of Titanium alloys. The basic difference between the two alloys besides composition was the size of the microstructure particles.

The Ti64 insert groups exhibited the familiar failure modes pertaining to WC/Co tools when milling titanium alloys. Chipping was noted along with carter wear. Chipping, however, was not observed for the Ti-x tool group.

For all rake angles used, the width of the delamination region, for the Ti-x tools, was observed to be slightly higher than that for the Ti64 alloy. The adhesion zone for the Ti-x tools was also found to be wider than that for the Ti64 tool group (except for the 5 degree rake angle tool).

We have attempted to explain the wear, and adhesion behaviour, observed on both tool groups based on a novel approach. This approach is based on the coupling between the thermal and electrical effects that take place in machining.

It was also found that the fine grain size of the Tix alloy may induce severe stresses due to reduced softening at higher temperatures and thus higher wear for inserts may be expected.

References

[1] R.R. Boyer, R.D. Briggs, J. Mater. Eng. Performance 14 (2005) 681–685

[2] J. Panter, A. Dallz, K.-H. Rendigs, N. Hellard, W. Gerhard, Influence of thermo-mechanical treatments on microstructure and mechanical properties of near beta titanium alloy VST 55531, Annual Meeting of the Materials Society, 2005

[3] S.L. Semiatin, V. Seetharaman, A.K. Ghosh, Plastic flow, microstructure evolution, and defect formation during primary hot working of titanium and titanium aluminide alloys with lamellar colony microstructures (1999), Philos. Trans. R. Soc. A: Math. Phys. Eng. Sci. 357 (1756) 1487−1512

[4] M. Jackson, R. Dashwood, L. Christodoulou, H. Flower, The microstructural evolution of near beta alloy Ti-10V-2Fe-3Al during subtransus forging, Metall. Mater. Trans. A: Phys. Metall. Mater. Sci. 36 (2005) 1317–1327

[5] M. Jackson, Application of novel technique to examine thermomechanical processing of near beta alloy Ti-10V-2Fe-3Al, Mater. Sci. Technol. 16 (2000) 1437−1444

[6] V.V. Balasubrahmanyam, Y.V.R.K. Prasad, Deformation behaviour of beta titanium alloy Ti-10V-4.5Fe-1.5Al in hot upset forging, Mater. Sci. Eng. A 336 (2002) 150–158

[7] N.G. Jones, R.J. Dashwood, D. Dye, M. Jackson, Mater. Sci. Eng. A 490 (2008) 369–377

[8] J.I. Hughes, A.R.C. Sharman, K. Ridgway, The effect of cutting tool material and edge geometry on tool life and workpiece surface integrity, Proc. Instit. Mech. Eng. B: J. Eng. Manufact. 220 (2006) 93–107

[9] E.O. Ezugwu, Z.M. Wang, Titanium alloys and their machinability – A review, J. Mater. Proc. Technol. 68 (1997) 262–274

[10] M.V. Ribeiro, M.R.V. Moreira, J.R. Ferreira, Optimization of titanium alloy (6Al-4V) machining, J. Mater. Proc. Technol. 143-144 (2003) 458–463

[11] M. Lee, Proc. Symp. Advances in processing Methods for Titanium, Louisville Kentucky, AIME, 1981, pp. 275–287

[12] P.C. Wanigarathne, A.D. Kardekar, O.W. Dillon, G. Poulachon, I.S. Jawahir, Progressive tool-wear in machining with coated grooved tools and its correlation with cutting temperature, Wear 259 (2005) 1215–1224

[13] Y.S. Touloukian, Thermophysical Properties of Matter – Metallic Elements and Alloys, John Wiley & Sons Ltd, NY, 1971

[14] H.A. Abdel-Aal, M. Nouari, M. El Mansori, Influence of thermal conductivity on wear when machining titanium alloys, Trib. Int. 42 (2009) 359–372

[15] H.A. Abdel-Aal, M. Nouari, M. El Mansori, Tribo-energetic correlation of tool thermal properties to wear of WC-Co inserts in high speed dry machining of aeronautical grade titanium alloys, Wear 266 (2009) 432–444

[16] N Wiser, Electrical resistivity of metals, in Encyclopedia of Physical Science and Technology, Academic Press, 1992, Vol. 5, p. 445

[17] H.A. Abdel-Aal, M. El Mansori, Influence of high pressure thermal behavior on friction-induced material transfer during dry machining of titanium, proc 14th Conference of (European Scientific Association for Material Forming) ESAFORM, Queen's University Belfast, Northern Ireland, April 27th to 29th, 2011, AIP Conf. Proc. 1353 (2011) 1806–1811

[18] H.A. Abdel-Aal, M. El Mansori, Dry reciprocating sliding of WC-Co and commercially pure tungsten on titanium under the influence of biasing dc-current, 13th International Conference on Metrology and Properties of Engineering Surfaces 2011 METPROP, National Physical Laboratory 12–14 April 2011, pp. 126–130

[19] M.Y. Friedman, E. Lenz, The effect of thermal conductivity of tool material on cutting forces and crater wear rate, Wear 25 (1973) 39–44

[20] Lenz and M.Y. Friedman, Investigation of the tool-chip contact length in metal cutting, Int. J. Mach. Tool Des. Res. 10 (1970) 401–416

[21] N.G. Jones, R.J. Dashwood, D. Dye, M. Jackson, Mater. Sci. Eng. A 490 (2008) 369–377

[22] P.S. Balog, R.A. Secco, High pressure and temperature behaviour of electrical resistivity of hcp metals Ti, Zr and Gd, J. Phys.: Condens. Matter 11 (1999) 1273